Changes in tropical precipitation intensity with El Niño warming

Sylvia C. Sullivan[1], Kathleen A. Schiro[2], Jiabo Yin[3], and Pierre Gentine[1]

[1]Department of Earth and Environmental Engineering, Columbia University
500 West 120th Street, 918 S. W. Mudd Hall, New York, NY 10027

[2]Jet Propulsion Laboratory, California Institute of Technology
4800 Oak Grove Dr., Pasadena, CA 91109

[3]State Key Laboratory of Water Resources and Hydropower Engineering Science, Wuhan University, Wuhan 430072 China

Key Points:

- For the deepest convective systems, precipitation rates > 10 mm h^{-1} become two times more likely during El Niño.
- The distribution of net gross moist stability shifts to lower values for these deepest systems during El Niño.
- Decreased net gross moist stability can be explained by strengthened large-scale ascent and free tropospheric drying.

Corresponding author: Sylvia C. Sullivan, `sylvia.c.sullivan@gmail.com`

Corresponding author: Pierre Gentine, `pg2328@columbia.edu`

This article has been accepted for publication and undergone full peer review but has not been through the copyediting, typesetting, pagination and proofreading process which may lead to differences between this version and the Version of Record. Please cite this article as doi: 10.1029/2020GL087663

Abstract

Mesoscale convection generates the majority of extreme precipitation in tropical regions. Changes to these precipitation intensities, P, with long-term modes of climate variability have been hard to assess because they are not well-represented in current climate models. Here we stratify a satellite climatology of convective systems by El Niño phase and cloud top temperature. We find that gains (losses) in high precipitation intensity ($\dot{P} >$ 10 mm h^{-1}) are largest for the deepest (least deep) systems during El Niño relative to La Niña. The surface temperature and wind changes that define El Niño manifest as surface flux changes but are not sufficient to explain these $\dot{P}$ trends. We explore also the dynamical component of precipitation generation with a vertical momentum budget. Mid-tropospheric drying in the vicinity of the deepest systems boosts instability and ascent rates during El Niño, while the strengthened large-scale ascent minimizes the drag force on their updrafts.

Plain Language Summary

In the tropics, the majority of high-intensity precipitation comes from the organization of multiple thunderstorms into a convective system. These systems are not yet well-represented in global models, and studies of how their precipitation changes with long-term modes of climate variability like the El Niño Southern Oscillation have been limited. Using long-term satellite data, we find here that the most intense precipitation becomes two times more probable for the deepest systems and 20% less probable for the least deep systems during El Niño. With a budget for the ascent rate within these systems, we illustrate how favorable moisture structure acts as a buoyancy source in the first case and unfavorable circulation acts as a buoyancy sink in the latter case.

1 Introduction

Much effort has been dedicated to understanding how tropical precipitation intensities will change with atmospheric warming. Radiative-convective equilibrium (RCE) must hold for the tropics as a whole with moist static energy (MSE) generated by surface heat fluxes and lost via atmospheric radiative cooling. This constraint can be used to explain the global mean increase of 2 to 3% K^{-1} in precipitation (Jeevanjee & Romps, 2018). The RCE paradigm loses its validity at the scale of a single convective system, where local temperature, humidity, and pressure velocities become the dominant factors (e.g. Neelin & Held, 1987; Sobel, 2007; Jakob et al., 2019).

These organized convective systems are not yet well-parameterized within large-scale models (Moncrieff et al., 2012). Existing observational studies indicate that such systems contribute up to 40% of extreme tropical precipitation and can explain the majority of recent tropical precipitation changes (Rossow et al., 2013; Tan et al., 2015). Along with recent changes due to increasing surface temperature, we would like to understand changes in the associated precipitation with dominant modes of tropical climate variability like the El Niño Southern Oscillation (ENSO). Not only do many models lack parameterizations of organized convection, but they also do not consistently represent ENSO (Guilyardi et al., 2008). In light of these limitations, and with a satellite record that now extends over almost four decades, we turn to observations to investigate long-term variability in precipitation from organized convection.

We have recently shown that convective systems of a given extent bring greater precipitation accumulation during El Niño relative to La Niña (Sullivan et al., 2019). In this study, we stratify not only by El Niño phase, but also by convective system depth, to understand the impact of both on precipitation intensity. Along with the RCE framework mentioned above, the Clausius-Clapeyron (CC) relation has often been used to explain changes with warming via the moisture holding capacity of the atmospheric boundary layer (e.g. Trenberth, 1999). While the CC rate of about 7% per degree of warming holds globally at a statistically significant level (e.g. O'Gorman & Schneider, 2009; Yin et al., 2018), dynamical factors drive much of the regional-scale differences in the precipitation response to warming (Pfahl et al., 2017).

Here, we explain how this dynamical factor manifests differently for precipitation intensities during El Niño versus La Niña, due both to changes in the strength of the meridional overturning and to changes in nearby free tropospheric humidity. These factors can be summarized within a vertical momentum budget, with the former acting as a sink and the latter as a source for vertical motion. Generally, the population of clouds determines the environmental relative humidity (RH) via detrainment and reevaporation, so that instability (hence, vertical motion) and RH are dependent and directly related (Romps, 2016). But recent studies indicate that the environment in proximity of more organized convection becomes drier (Wing & Cronin, 2015; Holloway et al., 2017). If environmental RH is prescribed, instability should increase as free tropospheric RH decreases (Seeley & Romps, 2015). We emphasize the importance of this interaction of moisture and instability for precipitation intensities from organized convection.

2 Materials and Methods

2.1 Data

Our analyses center on the Deep Convection Tracking (CT) Database from the International Satellite Cloud Climatology Project (ISCCP) between 1983 and 2008 with 3-hourly temporal and 30-kilometer spatial resolution (Rossow et al., 1996; Rossow & Schiffer, 1999). Geostationary satellites have identified convective systems using an extent criterion of equivalent radius r_{eq} of 90 km for cloud top temperature less than 245 K (cold cloud shield) and a convective core being further distinguished by a 220-K threshold. r_{eq} of the system is calculated from the surface area of the 30-km pixels covered by the cold cloud shield. Only systems between 30° N/S are retained. To define depths, we use the minimum cloud top temperature observed for a given system. Months with an Oceanic Niño Index (ONI) of $\gtreqless \pm 0.5$ are classified as El Niño and La Niña respectively. To control for seasonality but retain statistics, analyses below include only boreal winter, when ONI-defined El Niño/La Niña conditions are most frequent.

Precipitation intensities are taken from the Multi-Source Weighted-Ensemble Precipitation (MSWEP) (Beck, van Dijk, et al., 2017; Beck, Vergopolan, et al., 2017) version 2.2 at 0.5° spatial and 3-hourly temporal resolution again from 1983 to 2008. We choose this product because of its long temporal overlap with ISCCP CT, its high spatial resolution for collocation with individual systems, and its optimized merging that lends robustness over the oceans. The precipitation intensities within the minimum-to-maximum latitude-longitude subdomain defined in the ISCCP database for each system (under the cold cloud shield) are retrieved, and the pointwise maximum of this min-max lat-lon grid is recorded as $\dot{P}$. Thereafter, the 99th percentile of these values is referred to as $\dot{P}_{99}$. $\dot{P}$ is an instantaneous maximum precipitation intensity rather than one taken over the convective system life cycle, but this does not strongly affect our results as we perform analyses with the upper percentile of these values. Although recent studies show a large spread in observed precipitation extremes (e.g. Masunaga et al., 2019), both product merging within MSWEP and collocation with the independent ISCCP CT should make the trends here relatively robust to the precipitation values used.

ECMWF ERA-Interim reanalysis Version 2.0 data are used to collocate vertical profiles of pressure velocity, specific humidity, temperature, and pressure from 1983 to 2008 to the nearest degree latitude-longitude with the convective system cores (Dee et al., 2011). Values are downloaded for L60 model levels 26 to 57 from the ECMWF Integrated Forecasting System (IFS), corresponding to 1002 to 122 hPa for a surface pres-

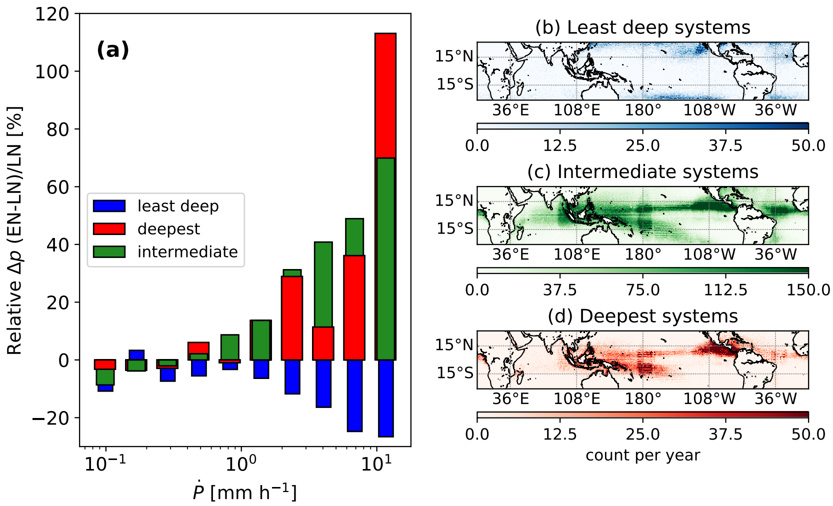

Figure 1. Probability distributions of relative differences in precipitation intensity $\dot{P}$ (panel a) between El Niño and La Niña for three cloud top temperature T_{top} classifications. The upper bound is set to 20 mm h^{-1}. Deepest systems have T_{top} colder than 215 K, intermediate with T_{top} between 215 and 240 K, and least deep systems with T_{top} warmer than 240 K. Counts in each bin are given in SI Appendix: Tab. S1, and mean T_{top} for each phase and depth are given in SI Appendix: Tab. S2. Heat maps of system occurrence for each depth are shown in panels b to d.

sure of 1013 hPa (ECMWF, 2018). Although the IFS and observations may not always produce convection at the same spatiotemporal location, we are primarily interested in sampling the large-scale convective environment rather than the immediate one.

2.2 Comparing Distributions

Histograms below are frequency-normalized and those that show relative differences are normalized by the La Niña value. For the probability distributions of surface flux and gross moist stability, the Kullback-Leibler divergence (D_{KL}) is used to quantify the El Niño-La Niña (EN-LN) difference. We calculate the KL divergence with the base-2 logarithm so that it can be interpreted as the bits lost when approximating the first distribution P by the second distribution Q:

$$D_{KL}(P||Q) = \sum_{x_i}^{x_n} P(x_i)\log_2\left(\frac{P(x_i)}{Q(x_i)}\right) \tag{1}$$

The KL divergence is not symmetric, so we use both $D_{KL}(p_{EN}||p_{LN})$ and $D_{KL}(p_{ELN}||p_{EN})$. The maximum number of bins with non-zero counts is used to compare each set of distributions, corresponding to $n = 45, 45, 40, 32$ in Fig. 2a, b, d, and e respectively.

3 Three Precipitation Responses to Surface Warming

Three clear changes appear in distributions of maximum precipitation intensity $\dot{P}$ between El Niño and La Niña (Fig. 1a, $\dot{P}$ defined in Methods: Data). First, high $\dot{P}$ (above 1 mm h^{-1}) is more probable, by as much as 20%, during La Niña relative to El Niño for the least deep convective systems. The opposite is true for systems of intermediate depth: high $\dot{P}$ is more probable during El Niño relative to La Niña. The deepest systems also show a relative gain in high $\dot{P}$ during El Niño but of much larger magnitude (up to 110%). These three responses are differentiated based on the system cloud top temperature T_{top}

(see Fig. 1 caption). The least deep systems generally form outside of the deep tropics, along the west coast of North America or in the western Atlantic (Fig. 1b). The intermediate systems form throughout the equatorial band (Fig. 1b-d), whereas the deepest ones are more longitudinally localized, clustering in the easternmost Pacific. During El Niño, occurrence of the intermediate systems concentrates dramatically within the warm tongue, while that of the deepest systems increases at its western margin and decreases over the warm pool (Fig. S1).

Distributional shifts are also clear from the absolute $\dot{P}$ distributions (Fig. S2), and the cloud top temperature thresholds correspond to only slightly different altitudes between El Niño and La Niña (Fig. S3). The observed behaviors in $\dot{P}$ with El Niño warming are also robust to the threshold cloud top temperatures within ± 2 K, changing bin numbers, and the histogram upper bounds (Figs. S4-S6). The mean horizontal extent quantified by an equivalent radius r_{eq} (Methods: Data) increases slightly as cloud top gets colder from 240 K down to 180 K (Fig. S7). This convective expansion occurs at approximately the same rate during both El Niño and La Niña and so cannot explain the EN-LN relative changes in $\dot{P}$. Given their robustness, the EN-LN distributional shifts in $\dot{P}$ raise two questions: first, why does large $\dot{P}$ become less frequent from the least deep systems during El Niño?; and second, why do the deepest systems exhibit the largest relative gains in extreme $\dot{P}$ during El Niño?

4 The Energy Budget for Precipitation

We begin by investigating the direct impact of sea surface temperature (SST) warming. As the east Pacific warms during El Niño, the east-west Pacific SST gradient weakens, in turn weakening the sea-level pressure gradient in the lower atmosphere. This atmosphere-ocean interaction has been well-established in the Bjerknes feedback. Indeed, collocated wind profiles show the slowing of the tradewinds during El Niño by up to 10% for all systems (Fig. 2c).

This deceleration extends down to the surface and reduces the probability of surface fluxes greater than about 600 W m^{-2} by 10 to 20% during El Niño (Fig. 2a-b). This reduction is of somewhat smaller magnitude for the deepest convective systems that form in the regions of warmest SST (Tab. S2). These warmer SSTs increase the saturation vapor mixing ratio and the rate of moisture transfer to the boundary layer. The decrease in surface flux can help us understand the $\dot{P}$ trends from the least deep systems but not the deepest ones.

While surface fluxes and radiative cooling act as energetic sources for precipitation at steady state, the efficiency with which these sources are converted may also change (Wang & Sobel, 2011; Anber et al., 2015). This surface flux efficiency, ∂P/∂SF is the inverse of the normalized gross moist stability (NGMS), which we define here as the ratio of moist to dry static energy divergence: $< \omega\partial_p h >/< \omega\partial_p s >$, where ω is pressure velocity, h is moist static energy, and s is dry static energy. The probability of NGMS less than 0.4 (high efficiency) is on average 20% more likely during La Niña for the least deep systems (Fig. 2d). The opposite is true for the deepest systems: their probability of low NGMS (< 0.4, high efficiency) decreases by 20% during La Niña, while their probability of high NGMS (> 0.7, low efficiency) increases by 20% during La Niña (Fig. 2e).

We quantitatively compare the EN-LN shifts in the distributions above using the Kullback-Leibler (KL) divergence (Methods: Scalings and histograms, values in Fig. 2a-b, d-e). For the least deep systems, the KL divergence between surface flux distributions is about 10% larger than that between the NGMS distributions. For the deepest systems, the KL divergence of the NGMS distributions is two times larger than that of the surface flux distributions. These values, along with the magnitude of the relative differences, show that EN-LN differences in both precipitation sources and their efficiencies cause

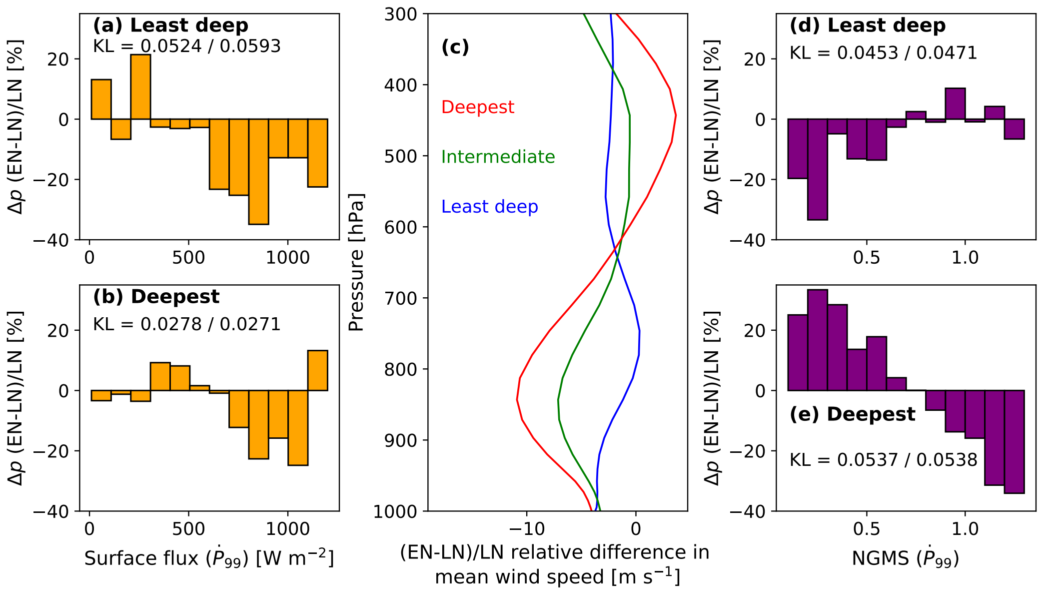

Figure 2. Probability distributions of the EN-LN relative differences in surface latent and sensible heat fluxes and normalized gross moist stability (NGMS) associated with $\dot{P}_{99}$ for the least deep systems (panels a and d) and for the deepest systems (panels b and e). Values of the Kullback-Leibler divergence are also given, first for the LN distribution from the EN one and then for EN from LN. The EN-LN relative difference in mean wind speeds collocated with the systems for all systems (panel c).

the distributional shifts in $\dot{P}$. We have used convective mass flux as the measure of convective strength within our NGMS calculation and proceed to investigate how and why it changes with El Niño phase.

5 The Momentum Budget for Ascent Rates

5.1 Large-scale Circulation as a Buoyancy Sink

From the mean pressure velocity profiles (Fig. 3a), and in agreement with the heat maps of occurrence (Fig. 1), the least deep systems tend to exist in an environment of large-scale descent, whereas the intermediate and deepest systems exist in regions of large-scale ascent. Profiles of the 1st percentile in pressure velocities also show that extreme ascent is stronger during El Niño than La Niña for the deepest systems (Fig. 3b), while the converse is true for the least deep systems.

To understand which factors set the convective updrafts associated with high precipitation intensity, we employ a vertical momentum budget. For cloudy updrafts w_c, the dominant force balance has been shown to be between buoyancy and pressure drag (de Roode et al., 2012; Romps & Charn, 2015) (derivation given in SI Appendix):

$$\frac{\partial w_c}{\partial t} = B - \frac{1}{\rho}\frac{\partial p'}{\partial z} \tag{2}$$

Calculating the terms of this balance, the least deep systems maintain positive buoyancy until 500 hPa with 2% increases during La Niña up to the 800 hPa level and 2 to 3% decreases above that. The pressure gradient force, analogous to drag, also decreases

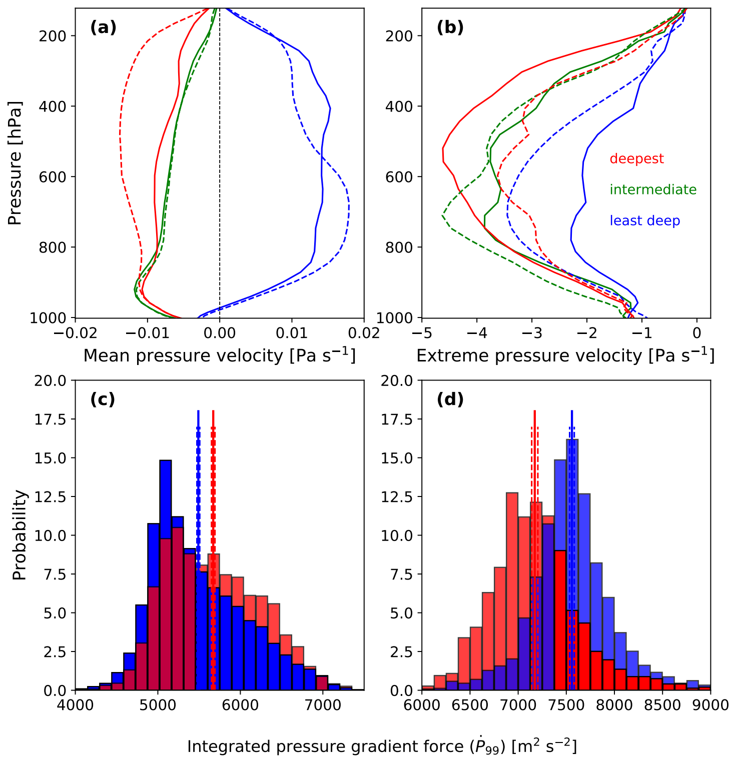

Figure 3. Mean collocated pressure velocity and extreme pressure velocities defined by the 1st percentile (negative values indicate ascent, panels a and b respectively). The deepest, intermediate, and least deep systems are shown in red, green, and blue for El Niño in solid lines and La Niña in dashed lines. Probability distributions of the integrated pressure gradient force, associated with $\dot{P}_{99}$, are also shown for the least deep and deepest systems (panels c and d respectively) with a solid line indicating the mean and dashed lines for the 99% confidence interval. Red indicates El Niño and blue La Niña.

at all levels during La Niña by 5 to 6%, twice as much as any buoyancy loss. Integrating these profiles, we see a relative gain of 5% in total drag during El Niño (Fig. 3c). This shift in the force balance weakens w_c for the least deep systems during El Niño. We see opposite trends from the same calculation for the deepest systems: a 5% relative decrease in total drag during El Niño corresponds to stronger ascent (Fig. 3d).

These shifts in pressure drag are consistent with the small, positive correlation of Hadley circulation strength with El Niño conditions, as reported in other studies (e.g. Oort & Yienger, 1996; Quan et al., 2004; Schwendike et al., 2014). Indeed, the meridional separation of the least deep and deepest systems (Fig. 1b-d) suggests that a change in the meridional overturning drives their opposing changes in drag force. For the least deep systems during El Niño, if the descending branch of this overturning strengthens, the force balance shifts to weaken their convective updrafts (Eq. 2). Weaker updrafts in turn diminish the integrated condensation rate and $\dot{P}_{99}$, as shown in scaling studies (Muller et al., 2011). On the other hand, as the ascending branch also strengthens, the force balance shifts to enhance convective updrafts and $\dot{P}_{99}$ for the deepest systems. But the relative loss and gain in $\dot{P}_{99}$ still exceed the respective gain and loss in pressure gradient force (Fig. 1a), indicating that another factor must be at play.

5.2 Free Tropospheric Drying as a Buoyancy Source

We next explore the buoyancy term in Equation 2 in more detail. Given that the deepest systems are relatively infrequent in comparison to the intermediate ones (Fig. 1c-d), we hypothesize that these may be understood with a zero-buoyancy plume (ZBP) model (Singh & O'Gorman, 2013; Singh et al., 2017). The ZBP model conceptualizes convection as a plume in which entrainment mixing shifts the lapse rate from a moist adiabat toward a dry adiabat, such that tropical in-cloud buoyancies tend to be small. If this entrainment (ε_u) is negligible for a given air parcel (the *undilute parcel*), its buoyancy increases in proportion to the deviation of specific humidity from the saturation value, or saturation deficit:

$$B = \varepsilon_u L_v (1 - RH) q^*_{ve} \tag{3}$$

where ε_u is the entrainment rate, L_v is the latent heat of vaporization, RH is the relative humidity, and q^*_{ve} is the environmental saturation vapor mixing ratio.

In collocated RH profiles, El Niño shows a strong drying, or increasing saturation deficit, relative to La Niña for the deepest systems, especially in the mid-troposphere (Fig. 4a). This larger saturation deficit corresponds to larger instability and higher ascent rates during El Niño. Here, the deep convective population, dominated by systems of intermediate depth, sets the lapse rate through the weak temperature gradient (Sobel et al., 2001). Then, the infrequent deepest systems can capitalize on the free tropospheric saturation deficit to produce extreme $\dot{P}$. We make this argument first based on the order-of-magnitude larger frequency of the intermediate systems relative to the deepest ones (Tab. S1) and secondly based on the higher temperatures and lower lapse rates in their vicinity (Fig. S8).

We calculate the integrated ZBP buoyancy from RH and temperature profiles collocated with the deepest systems when they produce $\dot{P}_{99}$ and find that it increases by a factor of 2 to 4 during El Niño relative to La Niña (Fig. 4b). This EN-LN difference in mean ZBP buoyancy is statistically significant at the 99% level. If we instead use the 3- or 6-hour preceding RH and temperature profiles, we see the same EN-LN buoyancy increase but of weaker magnitude, as the preceding profiles are less affected by subsidence drying (not shown).

We can decompose these integrated buoyancy changes into latent and sensible heating components by fixing the profile of the other variable (Fig. 4c). For the deepest systems, the integrated buoyancy gain is driven almost exclusively by RH until 600 hPa,

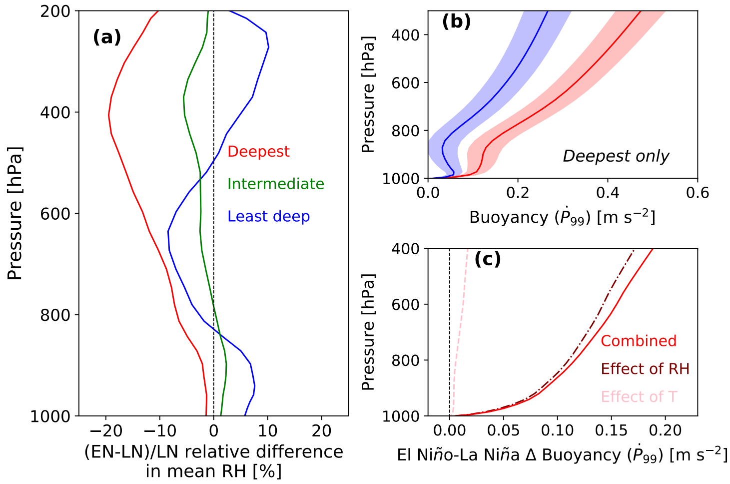

Figure 4. El Niño-La Niña relative difference in collocated RH profiles with the deepest, intermediate, and least deep systems in red, green, and blue respectively (panel a). ZBP model buoyancy profiles associated with $\dot{P}_{99}$ for the deepest systems with El Niño in blue and La Niña in red (panel b). The entrainment rate ε takes the form 1/z, and 99% confidence intervals for both phases are shaded. Decomposition of the EN-LN buoyancy differences in panel b into temperature and RH effects, shown in dashed pink and dotted-dashed maroon lines respectively (panel c).

above which a temperature contribution on the order of 10% appears. This upper-level temperature contribution reflects that these systems extend deep enough into the troposphere that the sensible heat component becomes important to their buoyancy (see also ZBP model section in the SI Appendix) (Seeley & Romps, 2015). In summary then, mid-level drying combine with warm SST and favorable circulation to produce the large gains in the high $\dot{P}$ from the deepest systems during El Niño.

6 Discussion

With multi-decade satellite data, we have shown how the distribution of precipitation intensities ($\dot{P}$) from organized convective systems changes with El Niño warming. Our study illustrates the utility of the satellite record, as we seek to develop large-scale parameterizations for these systems. The radiative-convective idealization does not hold at the scale of a single convective system (Jakob et al., 2019), and the computational cost of cloud-resolving models means that we cannot generally run them over tropics-wide domains for multiple years.

In an energetic budget, we find shifts not only in surface flux but also in the efficiency with which these sources translate to precipitation. The latter motivates a vertical momentum budget to investigate the shifts in the dynamics of precipitation generation. In this sense, our work corroborates a growing number of studies to emphasize the dynamical component, especially for convective precipitation (e.g. Pfahl et al., 2017; Nie et al., 2018). The vertical momentum budget gives insight into the complex relation of environmental moisture and convective precipitation that we do not have from a Clausius-Clapeyron scaling analysis. While increasing SST enhances the moisture holding capacity of overlying air, it also increases the saturation threshold. Sufficient low-level moisture is crucial to generate precipitation at all, but excess column-integrated moisture also reduces saturation deficit. Relative humidity determines the MSE surplus of undilute parcels (via the latent heating component) throughout much of the troposphere, but at the uppermost levels, SST can have an impact via the sensible heating component. The vertical momentum budget encapsulates these subtleties.

For the deepest systems during El Niño, we find that reduced drag from large-scale ascent, mid-level saturation deficit, and upper-level sensible heating components combine to generate a two-fold increase in the probability of $\dot{P} > 10$ mm h^{-1}. While such effect of large-scale circulation may be generalizable to isolated convection, the effects of anomalous drying here are likely limited to more organized convection. Long-channel RCE simulations indicate that free tropospheric drying increases as convection aggregates (Wing & Cronin, 2015; Holloway et al., 2017), and indeed we expect moist detrainment to decrease with the convective perimeter. Both the role of convective aggregation and microphysical precipitation efficiency are worth further investigation in this context.

Finally, recent work indicates that El Niño and its impacts, including localized heat extremes and wildfires, intensify as the surface warms (Fasullo et al., 2018). With the exception of the GFDL-ESM2M model (Kohyama et al., 2017), output of the Climate Model Intercomparison Projects indicates that El Niño occurrence increases under greenhouse gas forcing (Cai et al., 2014). It is becoming even more important then to understand how ENSO affects the tropics-wide distribution of precipitation intensities. How these distributional shifts depend on the flavor of El Niño as well as the propagation speed of convective systems also remain interesting open questions.

Acknowledgments

S.C.S. was partially supported by NSF Grant GG012658-01. Work by K.A.S. was carried out at the Jet Propulsion Laboratory, California Institute of Technology, under a contract with the National Aeronautics and Space Administration. Thanks to ECMWF and Hylke Beck at Princeton University for providing meteorological and precipitation data. Thanks also to two anonymous reviewers for their time and feedback that has improved this manuscript. We acknowledge Jacques Bodin-Hullin for SQL coding to assist with the collocation of meteorological and convective system data, Brahim Khalil Abid for initial organization of the convective tracking database, and Elzina Bala for helpful discussion. ISCCP convective tracking data are publicly available at https://isccp.giss.nasa.gov/outgoing/PICKUP/CT/. MSWEP precipitation data are available through the repository at www.gloh2o.org. ECMWF ERA-Interim reanalysis values are publicly available at www.ecmwf.int/en/forecasts/datasets/archive-datasets/reanalysis-datasets/era-interim. Scripts for collocation of convective systems and meteorological data are available at https://github.com/sylviasullivan. The authors declare no conflicts of interest.

References

Anber, U., Wang, S., & Sobel, A. (2015). Effect of surface fluxes versus radiative heating on tropical deep convection. *J. Atm. Sci.*, *72*, 3378–3388.

Beck, H. E., van Dijk, A. I. J. M., Levizzani, V., Schellekens, J., Miralles, D. G., Martens, B., & de Roo, A. (2017). MSWEP: 3-hourly 0.25-degree global gridded precipitation (1979-2015) by merging gauge, satellite, and reanalysis data. *Hydro. Earth Syst. Sci.*, *21*, 589-615. doi: 10.5194/hess-21-589-2017

Beck, H. E., Vergopolan, N., Pan, M., Levizzani, V., van Dijk, A. I. J. M., Weedon, G. P., … Wood, E. F. (2017). Global-scale evaluation of 22 precipitation datasets using gauge observations and hydrological modeling. *Hydro. Earth Syst. Sci.*, *21*, 6201-6217. doi: 10.5194/hess-21-6201-2017

Cai, W., Borlace, S., Lengaigne, M., van Rensch, P., Collins, M., Vecchi, G., … Jin, F.-F. (2014). Increasing frequency of extreme El Niño events due to greenhouse warming. *Nat. Clim. Change*, *4*, 111-116. doi: 10.1038/nclimate2100

Dee, D. P., Uppala, S. M., Simmons, A. J., Berrisofrd, P., Poli, P., Kobayashi, S., ... Vitart, F. (2011). The ERA-Interim reanalysis: configuration and performance of the data assimilation system. *Q. J. Roy. Meteorol. Soc.*, *137*, 553–597. doi: 10.1002/qj.828

de Roode, S. R., Siebesma, A. P., Jonker, H. J. J., & de Voogd, Y. (2012). Parameterization of the vertical velocity equation for shallow cumulus clouds. *Mon. Weather Rev.*, *140*, 2424–2436.

ECMWF. (2018). *Ifs Documentation - Cy45r1 Part IV: Physical processes.* Retrieved from https://www.ecmwf.int/node/18714

Fasullo, J. T., Otto-Bliesner, B. L., & Stevenson, S. (2018). ENSO's changing influence on temperature, precipitation, and wildfire in a warming climate. *Geophys. Res. Lett.*, 9216–9225. doi: 10.1029/2018GL079022

Guilyardi, E., Wittenberg, A., Fedorov, A., Collins, M., Wang, C., Capotondi, A., ... Stockdale, T. (2008). Understanding El Niño in ocean-atmosphere general circulation models: Progress and challenges. *Bull. Amer. Meteorol. Soc.*, 325–340. doi: 10.1175/2008BAMS2387.1

Holloway, C., Wing, A. A., Bony, S., Muller, C., Masunaga, H., L'Ecuyer, T. S., ... P.Zuidema (2017). Observing convective aggregation. *Surv. Geophys.*, *38*(6), 1199-1236.

Jakob, C., Singh, M. S., & Jungandreas, L. (2019). Radiative convective equilibrium and organized convection: An observational perspective. *J. Geophys. Res.*, *124*, 5418–5430.

Jeevanjee, N., & Romps, D. (2018). Mean precipitation change from a deepening troposphere. *Proc. Nat. Acad. Sci.*, *115*(45), 11465–11470. doi: 10.1073/pnas.1720683115

Kohyama, T., Hartmann, D., & Battisti, D. S. (2017). La Niña–like mean-state response to global warming and potential oceanic roles. *J. Clim.*, *30*, 4207–4225. doi: 10.1175/JCLI-D-16-0441.1

Masunaga, H., Schröder, M., Furuzawa, F. A., Kummerow, C., Rustemeier, E., & Schneider, U. (2019). Inter-product biases in global precipitation extremes. *Env. Res. Lett.*, *14*(12). doi: 10.1088/1748-9326/ab5da9

Moncrieff, M., Waliser, D. E., Miller, M. J., Shapiro, M. A., Asrar, G. R., & Caughey, J. (2012). Multiscale convective organization and the YOTC virtual global field campaign. *Bull. Amer. Meteorol. Soc.*, 1171–1188. doi: 10.1175/BAMS-D-11-00233.1

Muller, C., O'Gorman, P. A., & Back, L. E. (2011). Intensification of precipitation extremes with warming in a cloud-resolving model. *J. Clim.*, *24*, 2784–2800. doi: 10.1175/2011JCLI3876.1

Neelin, J. D., & Held, I. (1987). Modeling tropical convergence based on the moist static energy budget. *Mon. Weath. Rev.*, *115*, 3-12.

Nie, J., Sobel, A. H., Shaevitz, D. A., & Wang, S. (2018). Dynamic amplification of extreme precipitation sensitivity. *Proc. Nat. Acad. Sci.*, *115*(38), 9467–9472.

O'Gorman, P. A., & Schneider, T. (2009). The physical basis for increases in precipitation extremes in simulations of 21st-century climate change. *Proc. Nat. Acad. Sci.*, *106*(35), 14773–14777.

Oort, A. H., & Yienger, J. J. (1996). Observed interannual variability in the Hadley circulation and its connection to ENSO. *J. Clim.*, *9*, 2751–2767.

Pfahl, S., O'Gorman, P. A., & Fischer, E. M. (2017). Understanding the regional pattern of projected future changes in extreme precipitation. *Nat. Clim. Change*, *7*, 423–428. doi: 10.1038/nclimate3287

Quan, X.-W., Diaz, H. F., & Hoerling, M. P. (2004). Change in the tropical Hadley cell since 1950. In *The Hadley circulation: Present, past, and future.* Cambridge Univ. Press.

Romps, D. M. (2016). Clausius-Clapeyron scaling of CAPE from analytical solutions to RCE. *J. Atm. Sci.*, *73*, 3719–3737.

Romps, D. M., & Charn, A. B. (2015). Sticky thermals: Evidence for a dominant balance between buoyancy and drag in cloud udprafts. *J. Atm. Sci.*, *72*, 2890–2901.

Rossow, W. B., Mekonnen, A., Pearl, C., & Goncalves, W. (2013). Tropical precipitation extremes. *J. Clim.*, *26*, 1457–1466. doi: 10.1175/JCLI-D-11-00725.1

Rossow, W. B., & Schiffer, R. A. (1999). Advances in understanding clouds from ISCCP. *Bull. Amer. Meteor. Soc.*, *66*, 1498–1505.

Rossow, W. B., Walker, A. W., Beuschel, D., & Roiter, M. (1996). International Satellite Cloud Climatology Project (ISCCP): Description of new cloud datasets. *WMO/TD World Climate Research Programme (ICSU and WMO)*, *737*, 115.

Schwendike, J., Govekar, P., Reeder, M. J., Wardle, R., Berry, G. J., & Jakob, C. (2014). Local partitioning of the overturning circulation in the tropics and the connection to the Hadley and Walker circulations. *J. Geophys. Res. Atm.*, *119*(3), 1322–1339.

Seeley, J. T., & Romps, D. M. (2015). Why does tropical convective available potential energy (cape) increase with warming? *Geophys. Res. Lett.*, *42*, 10429–10437. doi: 10.1002/2015GL066199

Singh, M. S., Kuang, Z., Maloney, E. D., Hannah, W. M., & Wolding, B. O. (2017). Increasing potential for intense tropical and subtropical thunderstorms under global warming. *Proc. Acad. Nat. Sci.*, *114*(44), 11657–11662. doi: 10.1073/pnas.1707603114

Singh, M. S., & O'Gorman, P. A. (2013). Influence of entrainment on the thermal stratification in simulations of radiative-convective equilibrium. *Geophys. Res. Lett.*, *40*, 4398–4403. doi: 10.1002/grl.50796

Sobel, A. H. (2007). Simple models of ensemble-averaged precipitation and surface wind, given the sea surface temperature. In T. Schnieder, A. H. Sobel, & E. Lorenz (Eds.), *The global circulation of the atmosphere* (pp. 219–251). Princeton Univ. Press.

Sobel, A. H., Nilsson, J., & Polvani, L. M. (2001). The weak temperature gradient approximation and balance tropical moisture waves. *J. Atm. Sci.*, *58*, 3650–3665.

Sullivan, S., Schiro, K., Stubenrauch, C., , & P.Gentine. (2019). The response of organized convection throughout the tropics to El Niño warming. *J. Geophys. Res.*. doi: 10.1029/2019JD031026

Tan, J., Jakob, C., Rossow, W. B., & Tselioudis, G. (2015). Increases in tropical rainfall driven by changes in frequency of organized deep convection. *Nat.*, *519*, 451–455. doi: 10.1038/nature14339

Trenberth, K. E. (1999). Conceptual framework for changes of extremes of the hydrological cycle with climate change. *Clim. Change*, *42*(1), 327–339. doi: 10.1023/A:1005488920935

Wang, S., & Sobel, A. H. (2011). Response of convection to relative sea surface temperature: Cloud-resolving simulations in two and three dimensions. *J. Geophys. Res.*, *116*(D1119).

Wing, A. A., & Cronin, T. (2015). Self-aggregation of convection in long channel geometry. *Q. J. Roy. Meteorol. Soc.*, *142*(694), 1-15.

Yin, J., Gentine, P., Zhou, S., Sullivan, S. C., Wang, R., Zhang, Y., & Guo, S. (2018). Large increase in global storm runoff extremes driven by climate and anthropogenic changes. *Nat. Comm.*, *9*(4389). doi: 10.1038/s41467-018-06765-2

Figure 1.

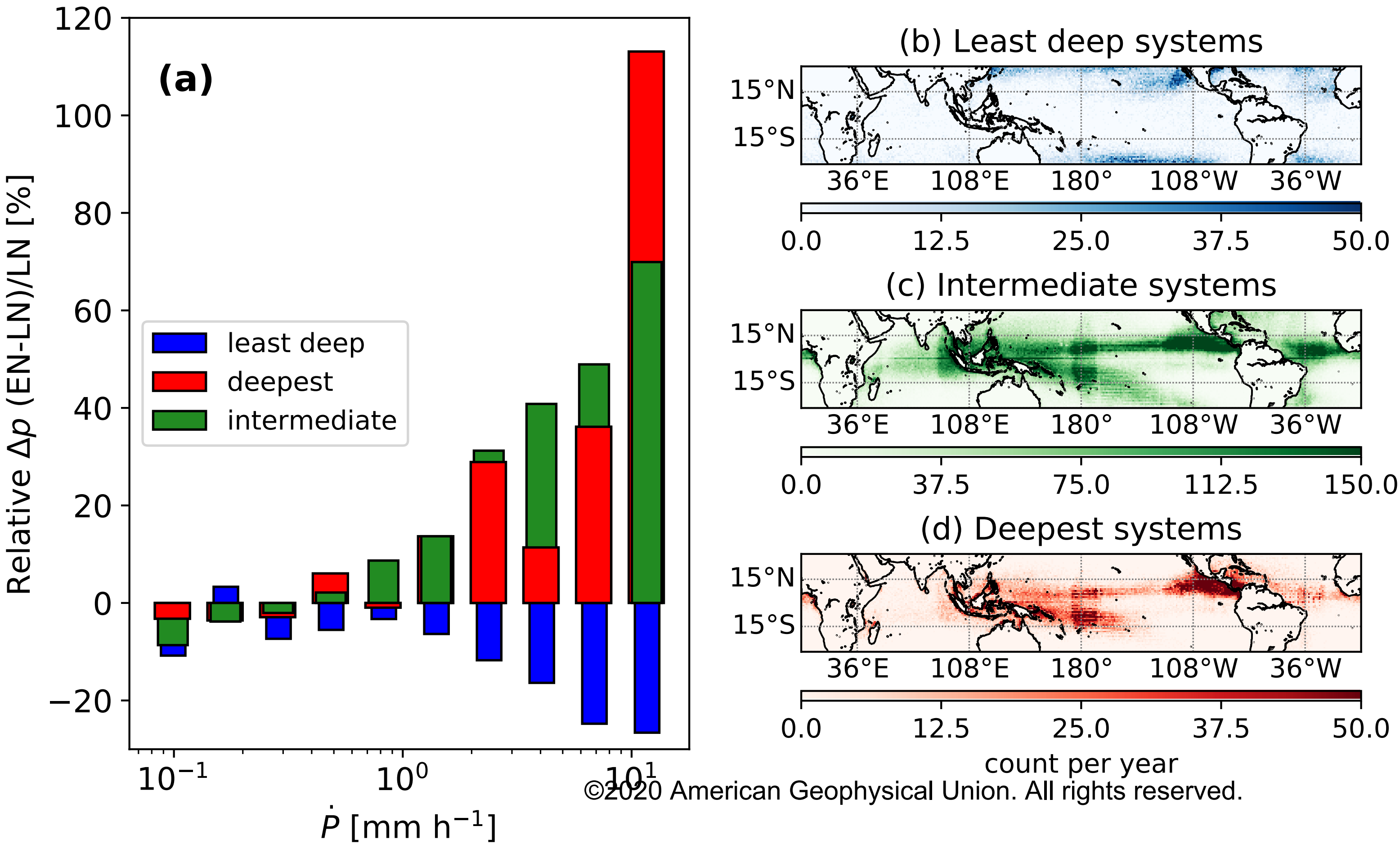
(a)
Relative Δp (EN-LN)/LN [%]
120
100
80
60
40
20
0
−20
least deep
deepest
intermediate
10^{-1}
10^{0}
10^{1}
$\dot{P}$ [mm h^{-1}]
(b) Least deep systems
15°N
15°S
36°E
108°E
180°
108°W
36°W
0.0
12.5
25.0
37.5
50.0
(c) Intermediate systems
15°N
15°S
36°E
108°E
180°
108°W
36°W
0.0
37.5
75.0
112.5
150.0
(d) Deepest systems
15°N
15°S
36°E
108°E
180°
108°W
36°W
0.0
12.5
25.0
37.5
50.0
count per year

Figure 2.

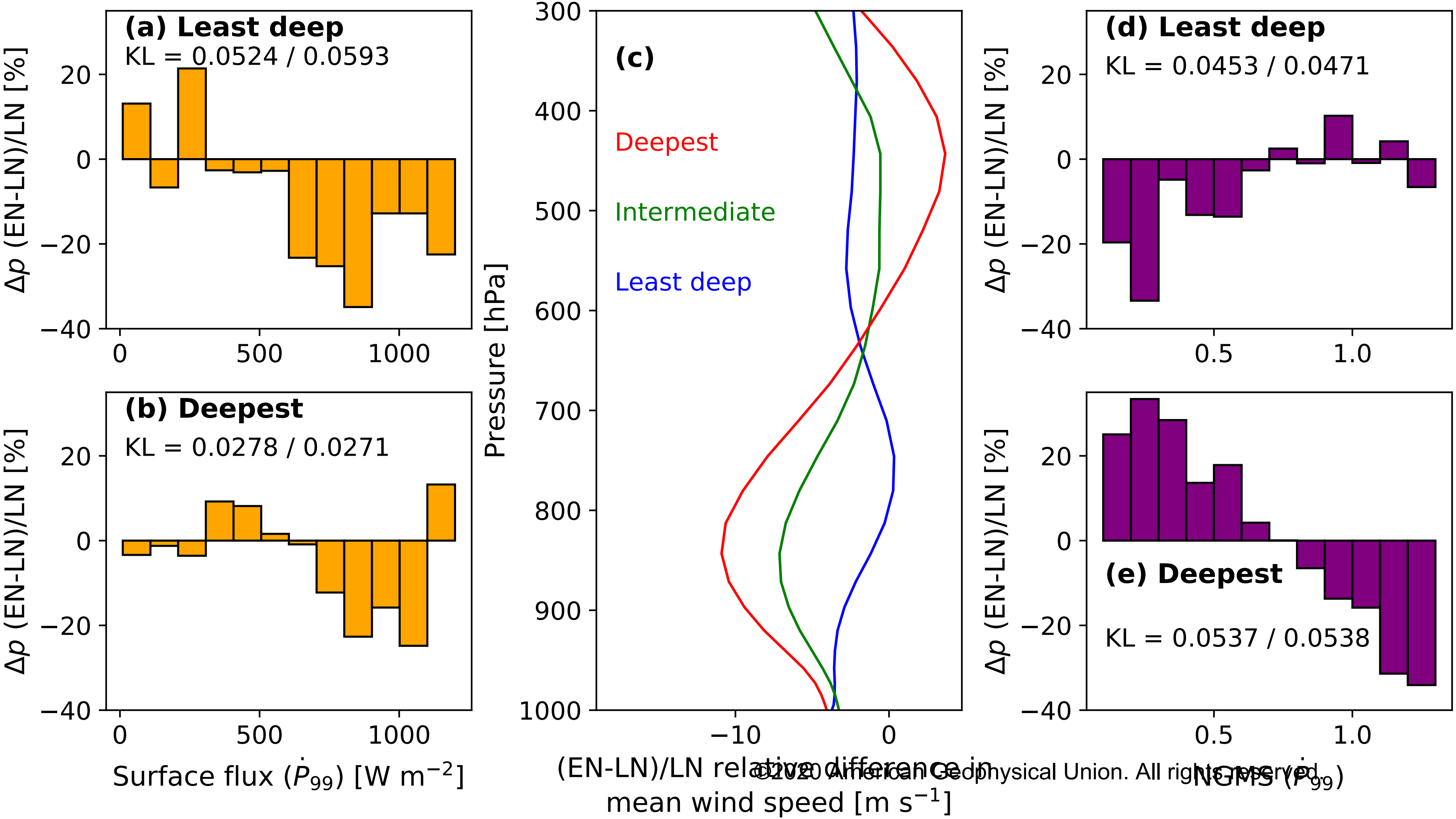
(a) Least deep
KL = 0.0524 / 0.0593
Δp (EN-LN)/LN [%]
(b) Deepest
KL = 0.0278 / 0.0271
Surface flux ($\dot{P}_{99}$) [W m^{-2}]
(c)
Deepest
Intermediate
Least deep
Pressure [hPa]
(EN-LN)/LN relative difference in mean wind speed [m s^{-1}]
(d) Least deep
KL = 0.0453 / 0.0471
(e) Deepest
KL = 0.0537 / 0.0538
NGMS ($\dot{P}_{99}$)

Figure 3.

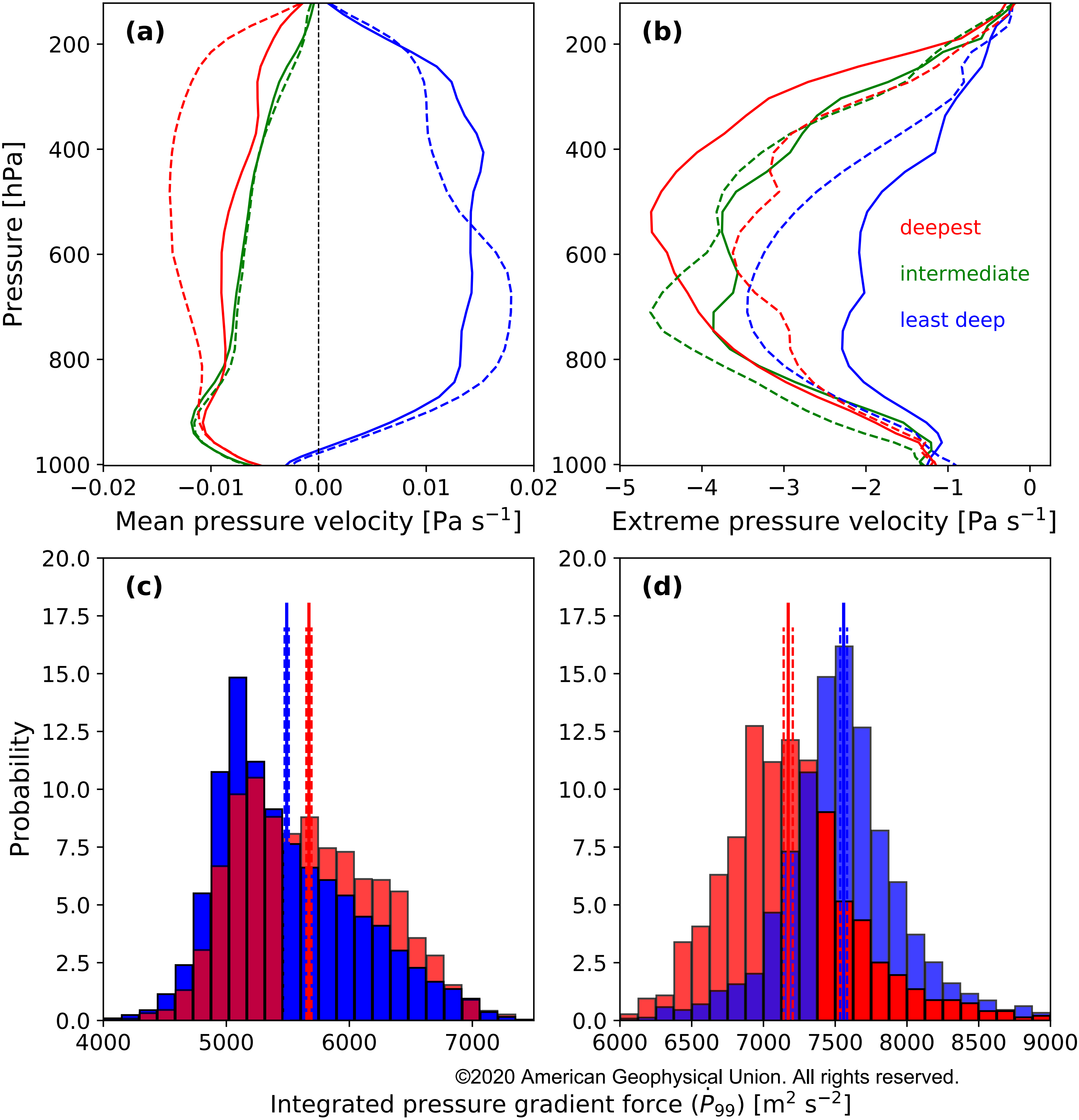
(a)
(b)
(c)
(d)
Pressure [hPa]
Mean pressure velocity [Pa s^{-1}]
Extreme pressure velocity [Pa s^{-1}]
deepest
intermediate
least deep
Probability
Integrated pressure gradient force ($\dot{P}_{99}$) [m^2 s^{-2}]

Figure 4.

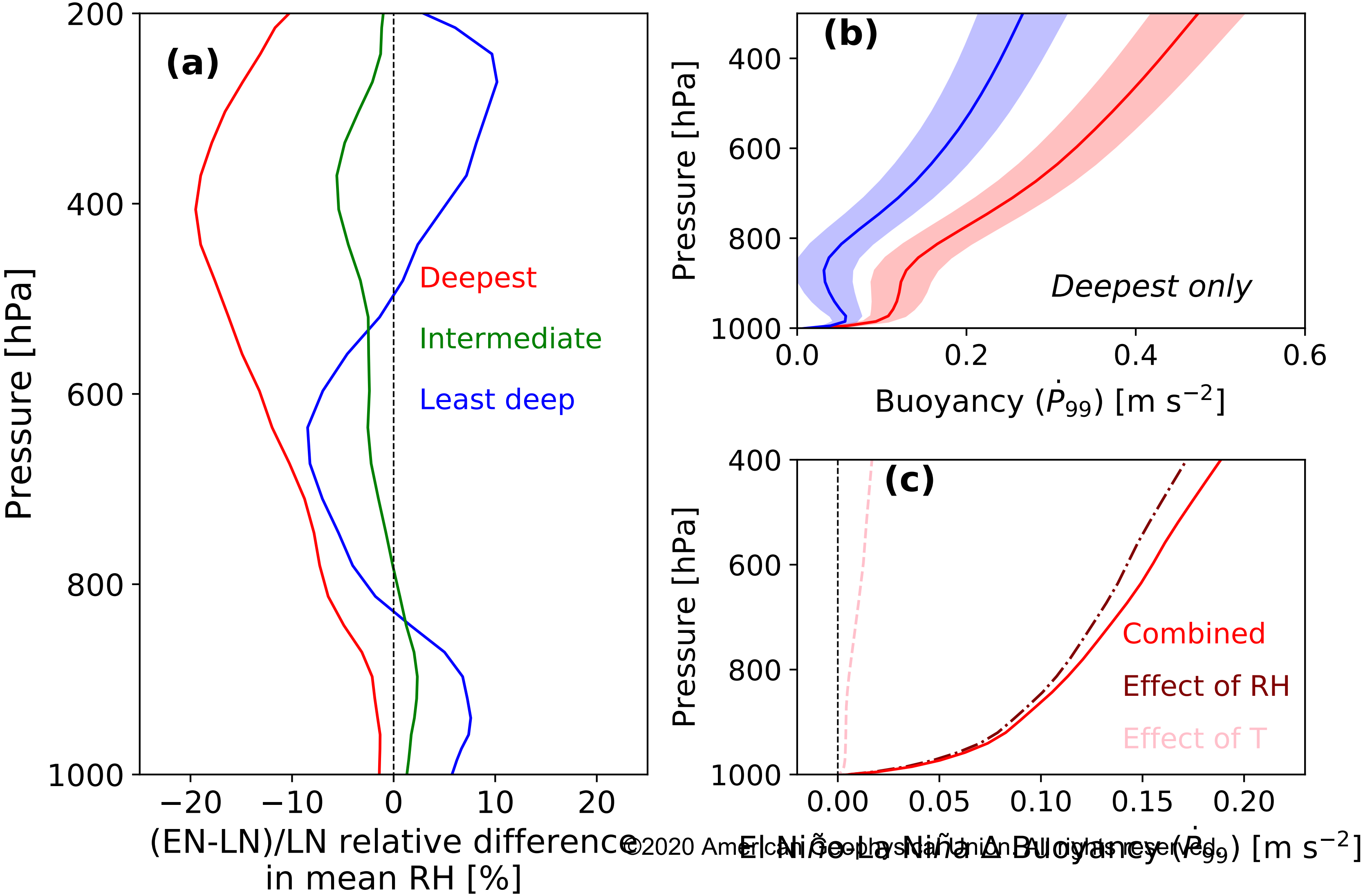
(a)
Pressure [hPa]
200
400
600
800
1000
−20
−10
0
10
20
(EN-LN)/LN relative difference
in mean RH [%]
Deepest
Intermediate
Least deep
(b)
Pressure [hPa]
400
600
800
1000
0.0
0.2
0.4
0.6
Buoyancy ($\dot{P}_{99}$) [m s^{-2}]
Deepest only
(c)
Pressure [hPa]
400
600
800
1000
0.00
0.05
0.10
0.15
0.20
El Niño-La Niña Δ Buoyancy ($\dot{P}_{99}$) [m s^{-2}]
Combined
Effect of RH
Effect of T

Figure S1.

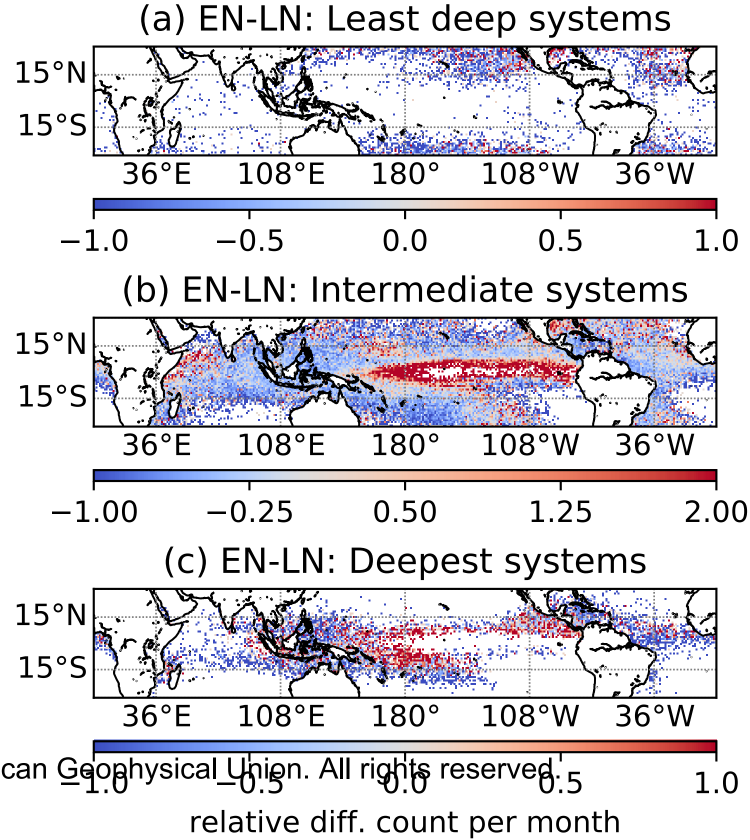
(a) EN-LN: Least deep systems
15°N
15°S
36°E
108°E
180°
108°W
36°W
−1.0
−0.5
0.0
0.5
1.0
(b) EN-LN: Intermediate systems
15°N
15°S
36°E
108°E
180°
108°W
36°W
−1.00
−0.25
0.50
1.25
2.00
(c) EN-LN: Deepest systems
15°N
15°S
36°E
108°E
180°
108°W
36°W
−1.0
−0.5
0.0
0.5
1.0
relative diff. count per month

Figure S2.

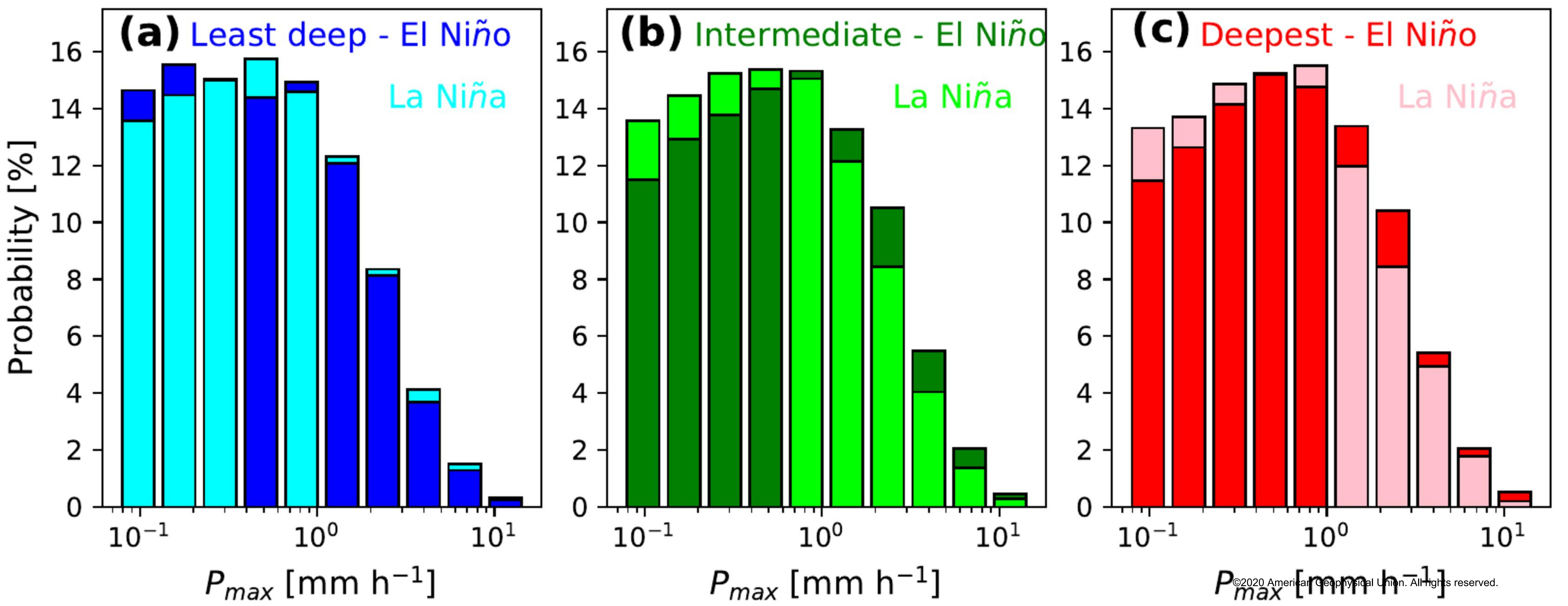

(a) Least deep - El Niño
La Niña
(b) Intermediate - El Niño
La Niña
(c) Deepest - El Niño
La Niña
Probability [%]
0
2
4
6
8
10
12
14
16
10^{-1}
10^{0}
10^{1}
P_{max} [mm h^{-1}]

Figure S3.

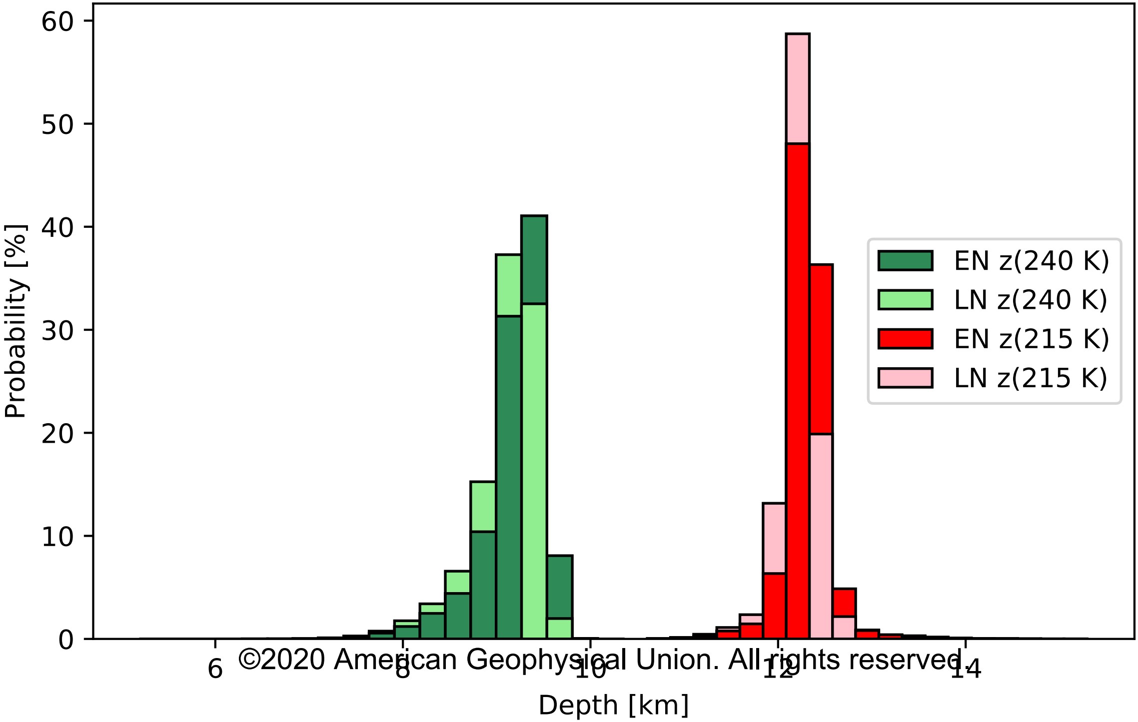

60
50
40
30
20
10
0
Probability [%]
6
8
10
12
14
Depth [km]
EN z(240 K)
LN z(240 K)
EN z(215 K)
LN z(215 K)

Figure S4.

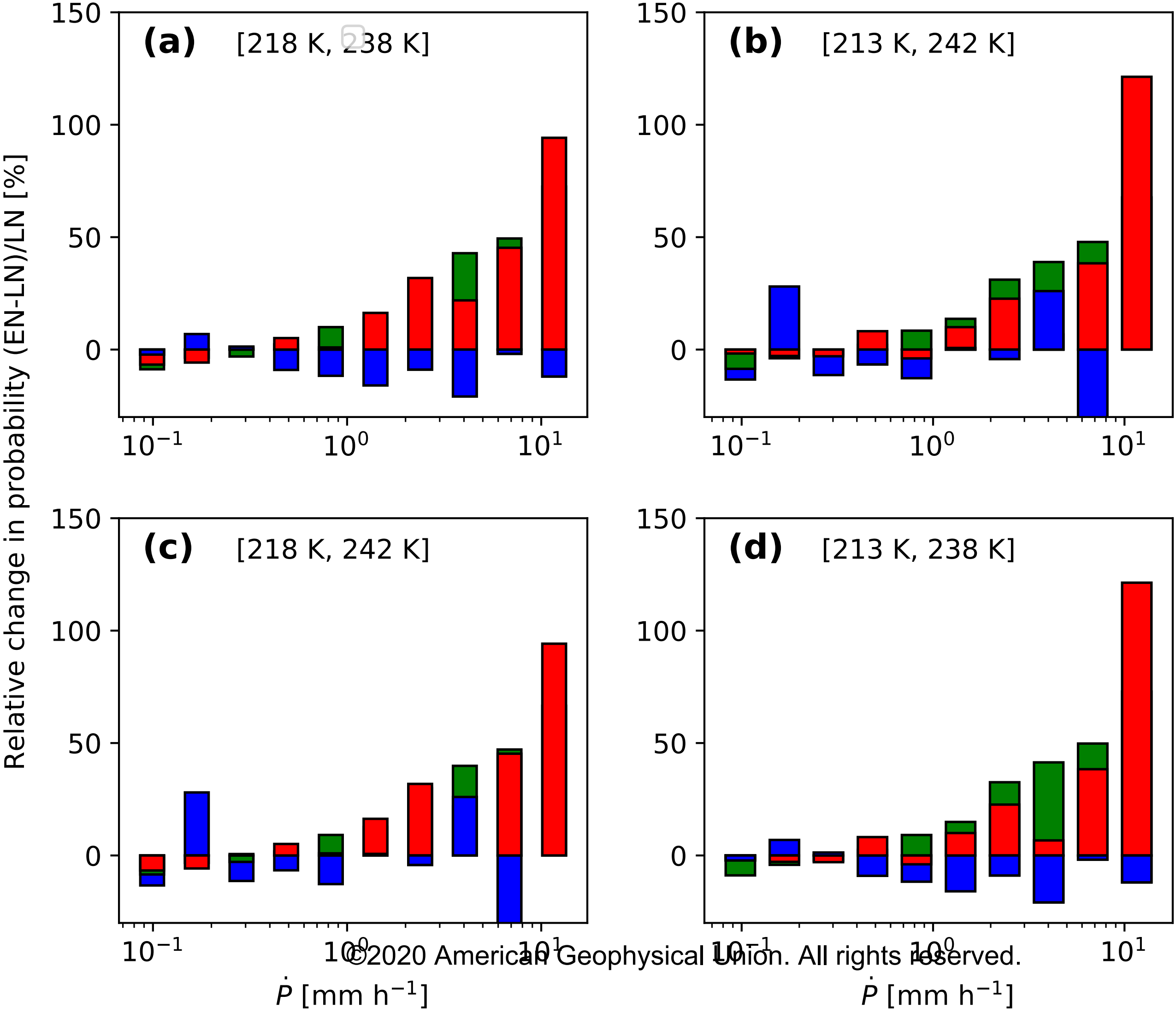

Relative change in probability (EN-LN)/LN [%]
(a) [218 K, 238 K]
(b) [213 K, 242 K]
(c) [218 K, 242 K]
(d) [213 K, 238 K]
150
100
50
0
10^{-1}
10^{0}
10^{1}
$\dot{P}$ [mm h^{-1}]

Figure S5.

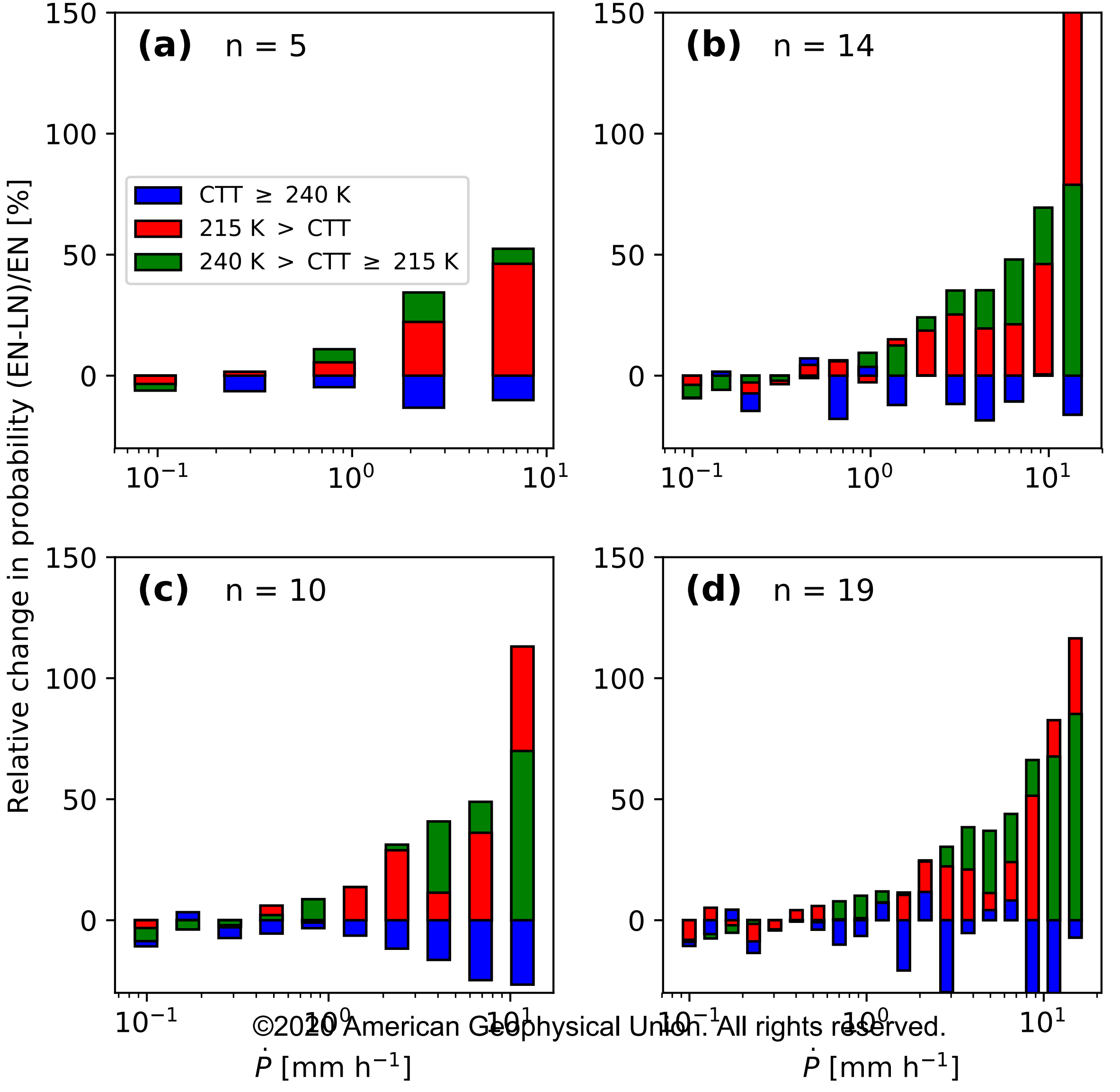
(a) n = 5
(b) n = 14
(c) n = 10
(d) n = 19
CTT ≥ 240 K
215 K > CTT
240 K > CTT ≥ 215 K
Relative change in probability (EN-LN)/EN [%]
$\dot{P}$ [mm h^{-1}]
$\dot{P}$ [mm h^{-1}]

Figure S6.

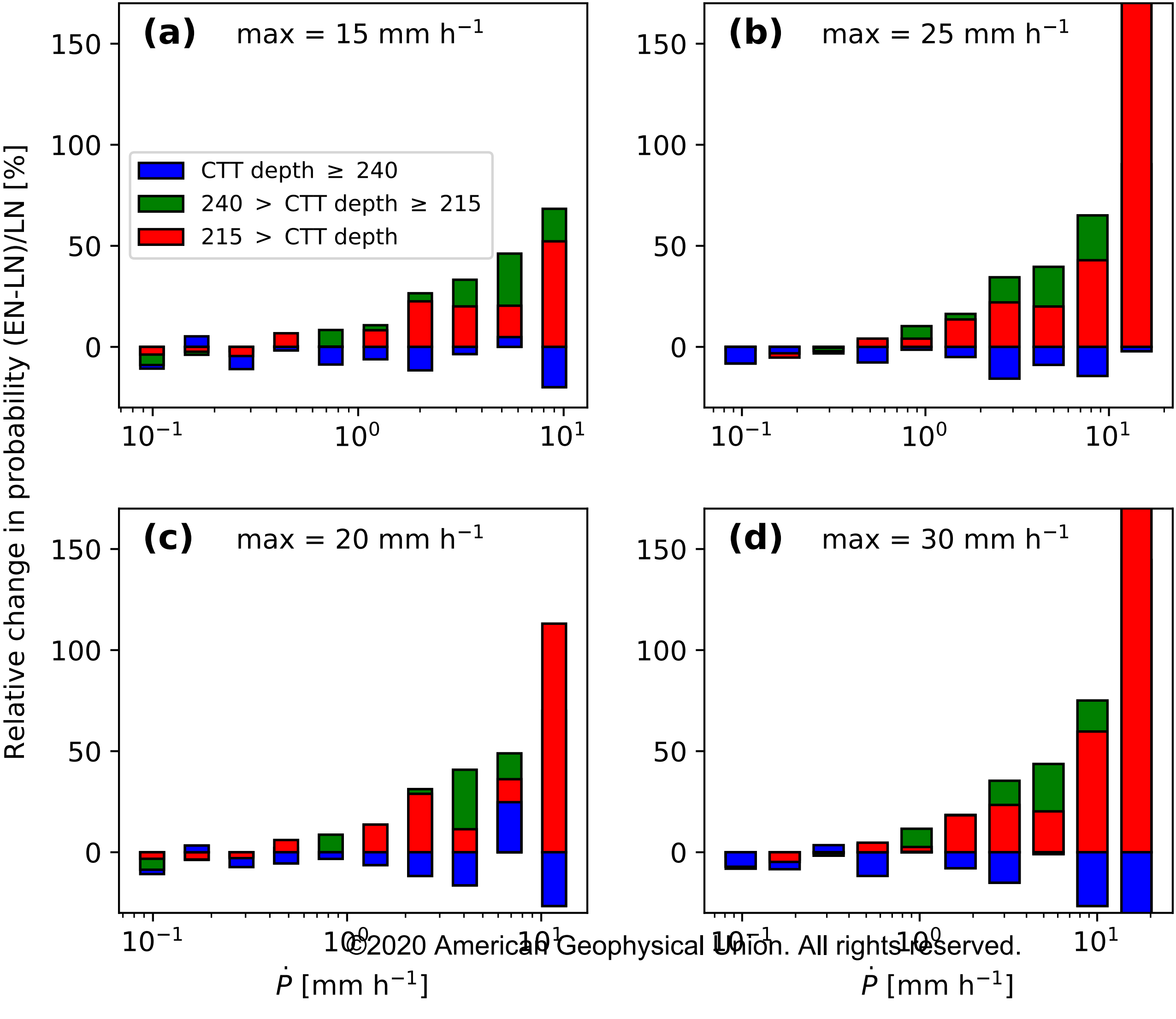

(a)
max = 15 mm h^{-1}
(b)
max = 25 mm h^{-1}
(c)
max = 20 mm h^{-1}
(d)
max = 30 mm h^{-1}
CTT depth ≥ 240
240 > CTT depth ≥ 215
215 > CTT depth
Relative change in probability (EN-LN)/LN [%]
$\dot{P}$ [mm h^{-1}]

Figure S7.

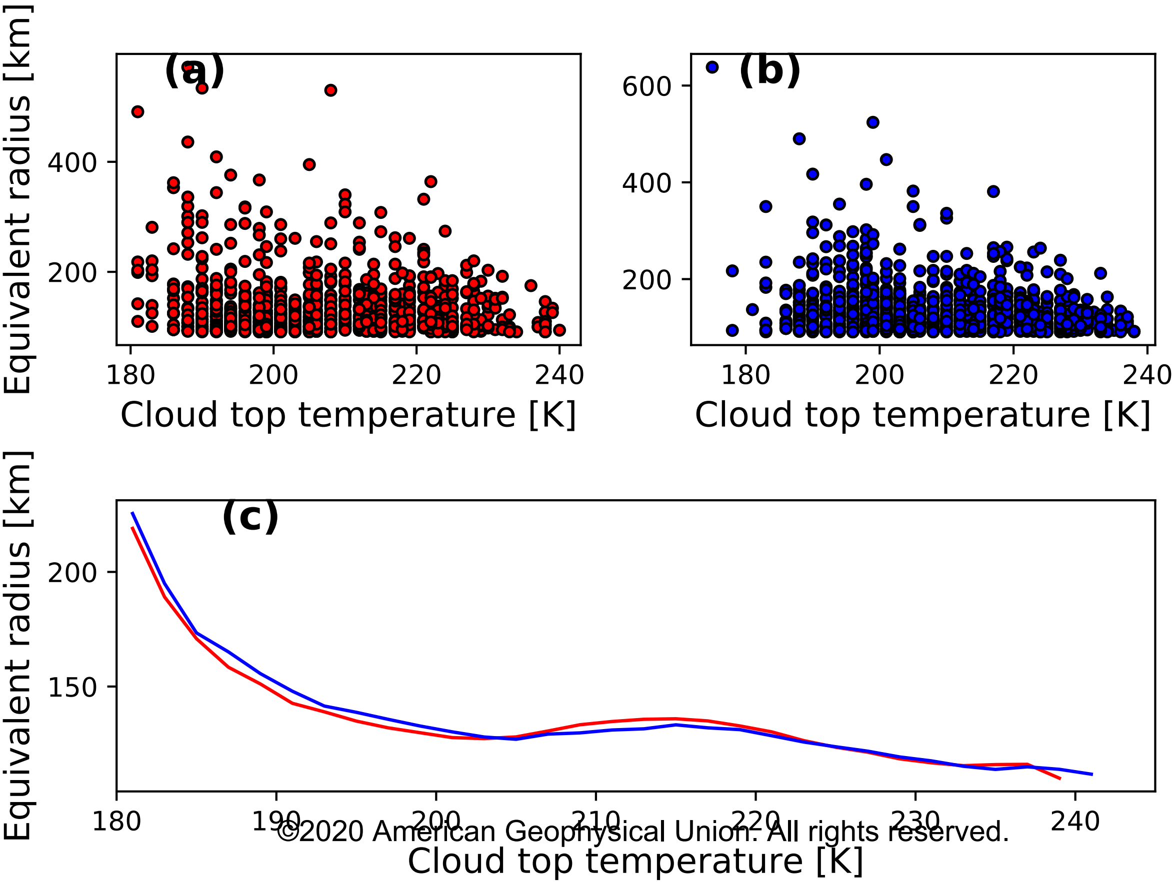
(a)
(b)
(c)
Equivalent radius [km]
Cloud top temperature [K]
180
190
200
210
220
230
240
150
400
600

Figure S8.

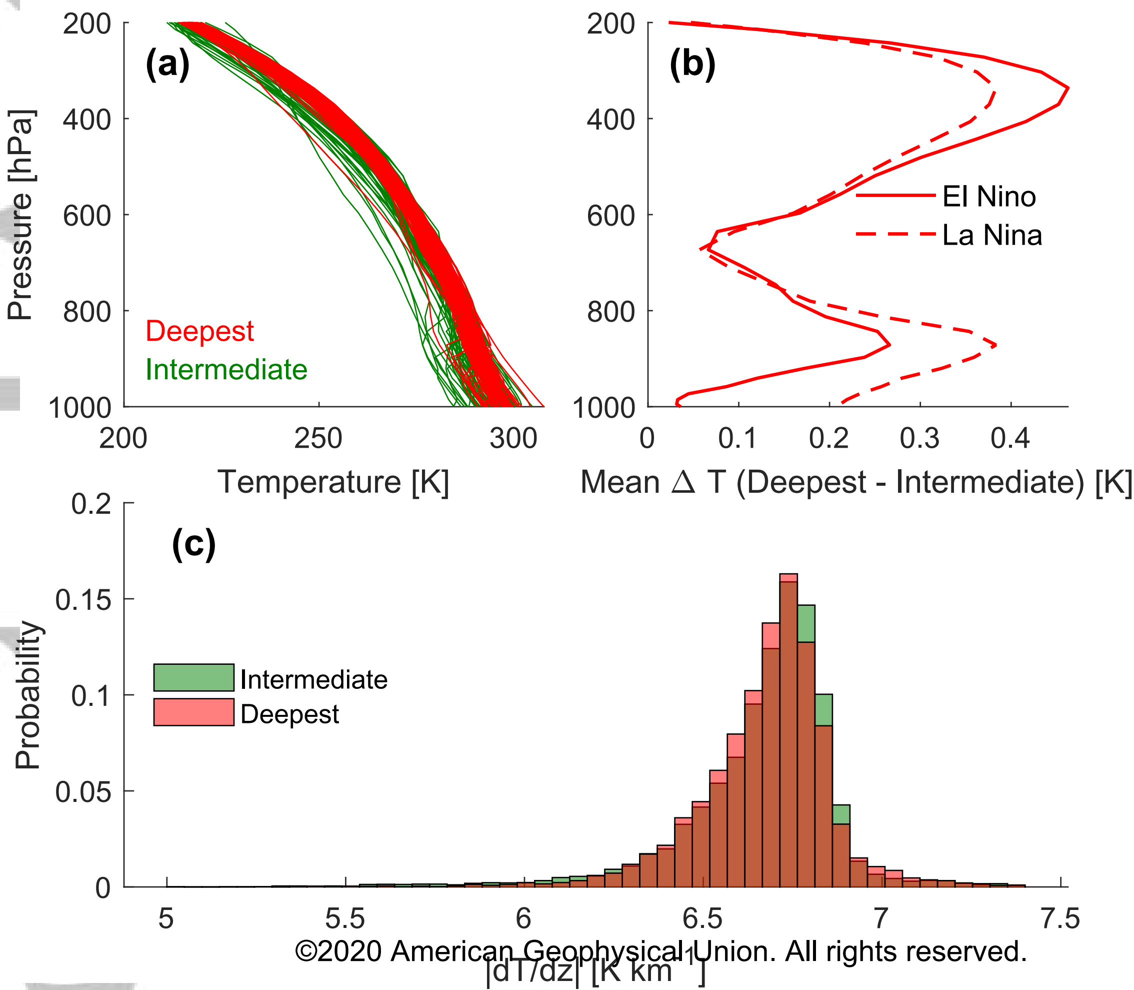

(a)
Pressure [hPa]
200
400
600
800
1000
Deepest
Intermediate
200
250
300
Temperature [K]
(b)
El Nino
La Nina
0
0.1
0.2
0.3
0.4
Mean Δ T (Deepest - Intermediate) [K]
(c)
Probability
0.2
0.15
0.1
0.05
0
Intermediate
Deepest
5
5.5
6
6.5
7
7.5
|dT/dz| [K km^{-1}]